Enhanced MOIDS-derived ice physical properties within CoLM revealing bare ice-snow-albedo feedback over Greenland

Shuyang Guo[1], Yongjiu Dai[1]*, Hua Yuan[1], Hongbin Liang[1]

[1] Southern Marine Science and Engineering Guangdong Laboratory (Zhuhai), School of Atmospheric Science, Sun Yat-sen University, Zhuhai, China

Corresponding author: Yongjiu Dai (daiyj6@mail.sysu.edu.cn)

Submitted to *The Cryosphere*

Abstract

Under global warming, the Greenland Ice Sheet (GrIS) is experiencing unprecedented mass loss. One key contributing factor is the change in snow and ice albedo, which is closely related to firn metamorphism. To investigate the impact of bare ice microstructure changes on the regional warming of the GrIS ablation zone, SNICAR-ADv4 (Snow, Ice and Aerosol Radiation model Adding-Doubling Version 4), a physically based radiative transfer model, is incorporated in Common Land Model version 2024 (CoLM2024). It allows the land surface model represent the ice albedo with changes in ice properties rather than using a constant ice albedo value. Quality control was conducted on the bare ice physical property dataset input into CoLM, with multiple MODIS products combined to ensure accuracy. The application of SNICAR-ADv4 reduced the overestimation of shortwave broadband albedo by 38%, with a bias of only 0.053. Further sensitivity experiments indicate that the summer albedo in the bare ice region is reduced by 0.032 due to the bare ice metamorphism, producing a 2-m temperature forcing of 0.071°C, a snow cover change of -0.011, and a snow water equivalent forcing of -1.345 mm. These changes lead to increased bare ice exposure, further reducing albedo and enhancing solar radiation absorption by the surface, thereby reinforcing a feedback involving bare ice, snow, and albedo. This highlights the critical role of bare ice physical properties in amplifying melt through the bare ice-snow-albedo feedback, with stronger feedbacks expected under a fully coupled land-atmosphere model.

Keywords

Greenland Ice Sheet; Bare ice region; Ice albedo; Albedo feedback; MODIS; Remote sensing

1. Introduction

The Greenland Ice Sheet (GrIS), the last remnant of the Ice Age has been melting at a rapid pace since the 1990s, losing around 255 Gt of ice annually in 2003-2016 (Sasgen et al., 2020; Li et al., 2022; van den Broeke et al., 2017). The negative mass balance of the GrIS and

peripheral glaciers is the most significant cryospheric factor driving sea level rise, contributing over 25% of observed global sea level rise (Chen et al., 2017; Ryan et al., 2019). Such melting was linked to a combination of processes including climate warming, reduced retention capacity of firn and lower surface albedo (Hofer et al., 2017; King et al., 2020; Ryan et al., 2024). The total mass loss from GrIS consists of two components: surface runoff and frontal ablation occurring at the terminus of outlet glaciers (Cogley et al., 2011, Kochtitzky et al., 2023). Surface losses have exceeded frontal losses in contributing to GrIS mass loss since 2000, with 55% of Greenland's total mass loss attributed to surface mass balance and 45% to the discharge of outlet glaciers between 2000-2018 (Mouginot et al., 2019).

Ice discharge on the surface of the GrIS is partially regulated by the surface albedo. It serves as a fundamental parameter in controlling the absorption of insolation by the ice sheet (Box et al., 2012; Naegeli et al., 2017, Feng et al., 2024). A minor change in snow and ice surface albedo can exert a substantial effect on the energy budget of regional surface-air system, causing significant fluctuations in the energy flux on the surface of the GrIS (Nolin and Stroeve, 1997). Surfaces with high albedo, such as fresh snow, efficiently reflect solar radiation, whereas darker areas, such as glacier ice, absorb the majority of incoming shortwave energy (Whicker-Clarke et al., 2022). Snow and ice albedo varies with the spatial distribution of snow, ice, and biotic and abiotic light absorbing constituents (LACs) and further evolves with the melting of snowpack and glacier surfaces through the spring and summer. Fluctuations in the snowline dictate the relative extent of dark bare ice versus brighter snow (Ryan et al., 2019). These directly influence GrIS surface melt through the exposure of bare ice (Antwerpen et al., 2022) and the processes that darken bare ice itself (Chevrollier et al., 2023). Dark bare ice extent closely tracks interannual variations in snowline elevation and is exposed as the snowline retreats further inland during the melt season, leading to the reduction of ice sheet albedo and the intensified melt. This positive feedback has been referred to as the "snow-albedo feedback" (Ryan et al., 2019).

In the preceding decades, polar amplification has contributed to the progressive darkening of

the GrIS and the prolongation of the melt season, both of which serve as positive feedback mechanisms that intensify surface melt (Tedesco et al., 2016). As the warming occurs over the ice surface, bare ice albedo is reduced through melt processes that darken the ice surface. Notably, these processes include exposure of dust layers, pooling of surface meltwater, increased interstitial water content, and liquid meltwater-induced growth of pigmented ice algal assemblages that inhabit the bare ice surface (Cook et al., 2020; Stibal et al., 2017; Tedstone et al., 2020; Williamson et al., 2018; Whicker-Clarke et al., 2022). Despite operating over a relatively small area of the ice sheet, it is argued that these bare ice processes have contributed substantially to an observed reduction in albedo and associated increase in melt across GrIS's ablation zone from 2000 to 2011 (Stibal et al., 2017; Tedstone et al., 2017). This category of physical and biological melt-albedo processes that darken bare ice is referred as the "bare ice-albedo feedback" (Ryan et al., 2019). However, the complex and non-linear response of regional snow and ice, particularly in ablation zones, to changes in meteorology and climate highlights the growing necessity to model these surfaces using physical principles rather than relying solely on empirical methods (Box et al., 2012). Therefore, accurately modeling the influence of snow and ice on the albedo of the GrIS becomes increasingly important to capture these dynamics effectively.

The albedo of the cryosphere varies widely depending on the solar zenith angle (SZA), atmospheric conditions, metamorphic state of the snow and ice, and impurities (He and Flanner, 2020). The Snow, Ice, and Aerosol Radiative (SNICAR) model is one of the most widely used snowpack radiative transfer models (Flanner et al., 2021). Initially, it combined the theory from Wiscombe and Warren (1980) and Warren and Wiscombe (1980) with the multi-layer two-stream solution from Toon et al. (1989) to enhance the simulation of snow albedo (Flanner et al., 2007). Updates and new features have also been incorporated within SNICAR, including eight species of LACs (Flanner et al., 2007), four snow grain shapes (He et al., 2018), black carbon-snow and dust-snow internal mixing state (Flanner et al., 2012; He et al., 2017, 2019). Dang et al. (2019) developed SNICAR-AD by substituting the tri-diagonal matrix solution solving method (Toon et al., 1989) with the delta-Eddington adding-doubling radiative method, as a result of the latter's superior computational stability

across varying solar zenith angles and higher computational efficiency (He et al., 2024). To represent ice albedo, Whicker-Clarke et al. (2022) further developed SNICAR-ADv4 by integrating and extending key features from earlier radiative transfer models to achieve more accurate simulations of a spectrally resolved cryospheric column of snow and ice with a refractive boundary, while incorporating light-absorbing constituents (LACs), such as black carbon (BC) and algae, into this standalone radiative transfer model. It simulates bare ice using the physical microscopic structure of the ice, including the ice density, the scattering air bubbles within an absorbing ice medium, and a refractive boundary that depicts the refraction across snow-ice interfaces (Briegleb and Light, 2007; Gardner and Sharp, 2010; Mullen and Warren, 1988).

Nevertheless, the ice albedo is typically prescribed as a constant value in the visible (VIS) and near-infrared (NIR) spectral regions in Earth system models (ESMs). For instance, Ice albedo is 0.6 in the visible and 0.4 in the NIR in the default version of the Energy Exascale Earth System Model (E3SM) and the Community Earth System Model (CESM) version 2 (Whicker-Clarke et al., 2024). Such parameterization does not capture the albedo of solid ice or variations in spectral albedo with changing ice conditions. To advance ice radiative transfer modeling in Earth system models (ESMs), Whicker-Clarke et al. (2024) incorporated SNICAR-ADv4 into the E3SM, in which the GrIS ice physical properties are retrieved by the satellite observation data. This enhancement enables more realistic simulations of the GrIS bare ice albedo, and concurrently reveals that the default ELM method overestimates bare ice albedo by 4% in the visible and 7% in the NIR bands. However, the quality information of MODIS albedo products were not considered in the process of acquiring bare ice properties in their study. Schaaf et al. (2011) noted that the MODIS poor-quality inversions beyond a SZA of 70° are characterized by high noise and often significantly lower than the more stable and consistent values observed at smaller SZAs. Omitting quality flags could, therefore, lead to an underestimation of Greenland's snow/ice albedo and introduce significant uncertainties in the retrieval of bare ice physical properties. Despite the aforementioned modeling advances, the Common Land Model (CoLM) still uses fixed values to represent ice albedo (0.60 in the visible and 0.40 in the NIR). For the purpose of investigating the impacts of bare

ice metamorphism under polar warming, it is also imperative to incorporate ice radiative transfer techniques into CoLM to enhance albedo modeling with more realistic and physical representations of snow-ice-LAC-radiation interactions.

In this study, we focus on the bare ice region of the GrIS, characterized by the presence of land ice, and bare ice is exposed with snow melting during ablation season. The aim of this study is to develop a more reliable dataset of Greenland's bare ice physical properties by incorporating the quality information of MODIS albedo products, and explore the bare ice-albedo feedback associated with the metamorphism of bare ice after the implementation of the SNICAR-ADv4 into the CoLM. This paper is organized as follows. Section 2 provides descriptions of the CoLM snow and ice albedo schemes and details the model simulations, as well as the explanation of the use of various MODIS products to inform the ice albedo calculations in SNICAR-ADv4. Section 3 compares the differences in albedo simulations with and without ice radiative transfer solver (SNICAR-AD and SNICAR-ADv4), and quantified the impact of varying bare ice properties on the near-surface air temperature and the snow cover. Section 4 is conclusions and discussion.

2. Models, Data, and Methods

2.1 Snow and Ice Albedo Scheme

This study utilizes two distinct implementations of the SNICAR model within the CoLM for snow and ice albedo simulations: (i) the baseline SNICAR-AD version (Dang et al., 2019) and (ii) the enhanced SNICAR-ADv4 version (Whicker-Clarke et al., 2024). Both versions adopt identical snow albedo algorithms but exhibit distinct ice albedo treatments. Specifically, as shown in Figs. 1a and b, the SNICAR-ADv4 accounts for radiative transfer through the ice column, while the SNICAR-AD prescribes ice albedo as constant values: 0.6 for visible (VIS: 0.3–0.7 μm) and 0.4 for near-infrared (NIR: 0.7–5.0 μm) bands. The snow albedo scheme of SNICAR-AD/SNICAR-ADv4 in the CoLM computes snow albedo for the multi-layer (up to 5 layers) snowpack with the two stream radiative transfer scheme of the delta-Eddington

160 approximation and adding-doubling technique, accounting for the effects of snow properties

161 (e.g., size and shape) and LAC contamination on snow albedo.

162
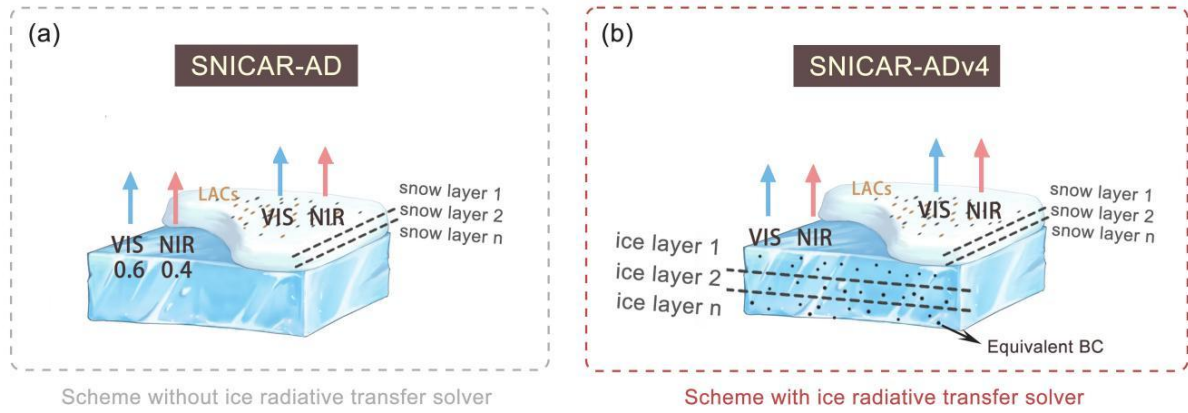
163 **Figure 1.** Schematic representation of the snow and land ice column in CoLM SNICAR-AD

164 and SNICAR-ADv4.

165

166 For snow albedo simulation, the SNICAR-AD/SNIACR-ADv4 embedded in CoLM uses the

167 physical properties of the snowpack and albedo of the top layer of the underlying ground to

168 determine the column albedo (Flanner and Zender, 2006). The input variables consist of

169 direct and diffuse radiation, the surface downward solar spectrum, the solar zenith angle (for

170 direct radiation), the ground albedo beneath the snowpack, vertical profiles of snow grain size,

171 snow layer thickness and density, aerosol concentrations of each snow layer, as well as the

172 optical properties of both snow and aerosols. Meanwhile, parameterizations for snow grain

173 shapes (sphere, spheroid, hexagonal plate, and Koch snowflake) and LACs-snow mixing

174 states (BC/dust externally or internally mixed with snow grains) are included to improve the

175 simulations of snow surface energy and water balances (Hao et al., 2023).

176

177 For ice albedo modeling, the advent of the SNICAR-ADv4 enables us to explore the regional

178 climatic response induced by changes in ice albedo using the ice microphysical properties

179 derived from satellite products. As proposed by Whicker-Clarke et al. (2024), the radiation

180 transfer process within the ice layer can be calculated in the land surface model, which

181 requires input variables such as ice density, air bubble effective radii within the ice,

182 equivalent BC concentrations, and downward solar spectra. The need for air bubble

parameters arises from the representation of ice layers as collections of independently scattering air bubbles within a solid ice medium in SNICAR-ADv4, while snow layers are treated as independently scattering ice crystals in an air medium (Picard et al., 2016; Whicker-Clarke et al., 2022).

2.2 Data

MODIS MCD12C1, MOD09CMG, and MOD10C1 products with consistent 0.05° spatial resolution were utilized for GrIS bare ice monitoring during the summer melt seasons of 2000-2020. The MCD12C1 Version 6.1 annual land cover type product (Friedl et al., 2010) provided initial cryospheric classification by excluding grids not categorized as snow or ice. The MOD09CMG (Vermote 2021) band 2 reflectance (0.841–0.876 μm) was employed for bare ice-snow discrimination, where pixels with reflectance values below 0.6 were classified as bare ice. Comparative spectral analysis of MODIS imagery by Shimada et al. (2016) revealed markedly greater surface reflectance in snow-covered pixels relative to bare ice across all spectral bands, with maximal contrast observed at 0.86 μm. The robustness of this threshold was confirmed by Antwerpen et al. (2022) through comparison with Landsat 8 OLI (Operational Land Imager), with a relative error of 0.16%. The MOD10C1 product was further used to exclude pixels with cloud obstruction percentage exceeding 90% or snow cover fraction above 90% (Antwerpen et al., 2022; Whicker-Clarke et al., 2024). The derived bare ice extent was filtered by excluding pixels above the mean equilibrium line altitude of 1679 m a.s.l., defined as the 95th percentile of ablation zone elevations. This conservative threshold minimizes sporadic high-elevation detections while maintaining robust estimation of the mean equilibrium line altitude (Antwerpen et al., 2022).

The MODIS MCD43C3 product (Schaaf et al., 2002) is used to retrieve bare ice physical properties by using standalone SNICAR-ADv4 and evaluate CoLM-simulated albedo over the GrIS bare ice regions. This daily product provides spectral (MODIS bands 1 to 7) and broadband (VIS 0.3–0.7 μm, NIR 0.7–5.0 μm and shortwave 0.3–5.0 μm) black-sky albedo (BSA) and white-sky albedo (WSA) at local solar noon, derived from 16 days of Aqua-Terra merged surface albedo dataset based on the bidirectional reflectance distribution function

212 (BRDF) algorithm (Schaaf and Wang, 2021). Among the GLASS-AVHRR and C3S-v2

213 albedo products, MCD43C3 stands out as the most reliable for monitoring snow albedo,

214 exhibiting the lowest bias and RMSE over snow and consistent performance across diverse

215 snow cover conditions (Urraca et al., 2022). In the GrIS, MCD43A3 was found to outperform

216 the GLASS albedo product and even the reconstructed albedo based on the MOD10A1, for

217 the sites located in the GrIS ablation zone (Ye et al., 2023).

218

219 Considering the little difference between BSA and WSA for a typical summer day, using

220 BSA is considered acceptable for analyzing the GrIS during the summer (Alexander et al.,

221 2014; Stroeve et al., 2005). The extracted variables in this study from MODIS MCD43C3

222 include Band 2 BSA, broadband BSA (visible, near-infrared and shortwave), along with local

223 noon solar zenith angles (SZAs) and albedo quality index. The MCD43C3 albedo quality

224 index helps identify regions with cloud cover contamination, detrimental atmospheric

225 conditions, or insufficient observational data. Figure 2a shows the daily variation of the

226 regionally weighted average SZA over Greenland during May-September. The period with

227 SZA>70° occurs primarily in September. For the relationship between the SZAs of

228 MCD43C3 and their spatiotemporally corresponding albedo quality index (Fig. 2b), it can be

229 seen that the percentage of low-quality indices (4 and 5) rises drastically as the SZA increases

230 at higher SZA. Therefore, we excluded albedo values identified with a low-quality index

231 when the SZA exceeded 70° to derive more reliable satellite-retrieved bare ice physical

232 properties.

233
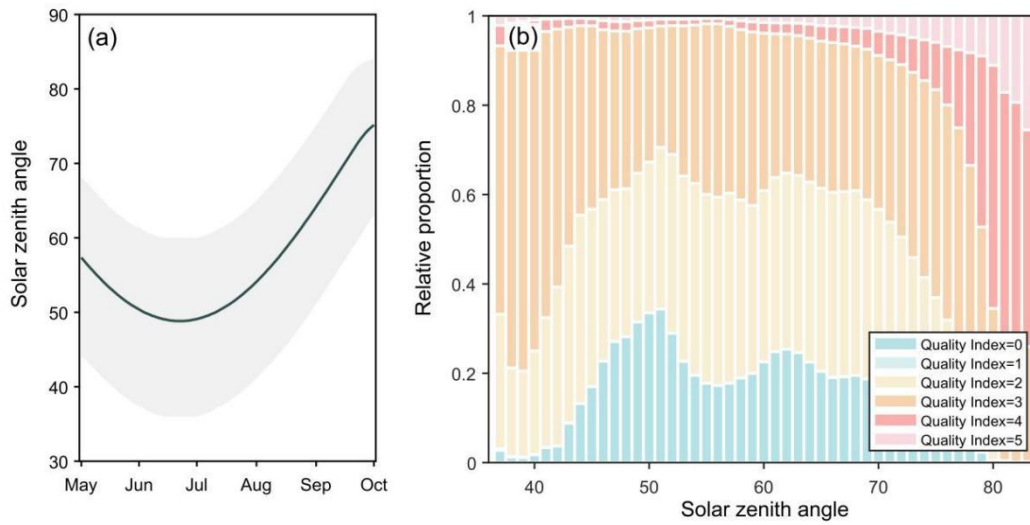
Figure 2. Regional-weighted mean SZAs of Greenland at local noon from May to September (a; solid line). Grey shaded area represents the range of SZAs over Greenland. Relative proportion of the quality index of MCD43C3 albedo dataset under different SZAs over Greenland during May to September (b; 0 for best quality and 5 for poorest quality)

2.3 Method

The method for obtaining ice physical properties (ice density, air bubble effective radius and equivalent BC) from MODIS bare ice albedo involves two main steps (Whicker-Clarke et al., 2024). First, as detailed in Section 2.2, bare ice spatiotemporal distribution was determined through the integrated use of MODIS products, employing MCD12C1 to exclude non-cryospheric pixels, MOD09CMG to distinguish bare ice from snow cover, and MOD10C1 to apply snow and cloud masking. Second, the bare ice physical properties (ice density and air bubble effective radius) are retrieved using MCD43A3 band 2 BSA and its corresponding SZA to match the closest physical properties within the precomputed lookup table by standalone SNICAR-ADv4 model. Notably, this step derives only ice density and air bubble effective radius, whereas equivalent black carbon (BC) concentration requires additional processing steps described later in this section. After obtaining all bare ice physical properties (ice density, air bubble effective radius, and equivalent BC concentration), we upscaled the data from a spatial resolution of 0.05°×0.05° to 0.5°×0.5°.

252

253 The lookup table was generated using the standalone SNICAR-ADv4 radiative transfer

254 model by testing a range of parameter combinations within physically constrained ranges,

255 including ice density (650-916 kg·m⁻³) and air bubble radii (100-1500 μm), as well as the

256 SZAs spanning 35° to 75° to represent typical local noon conditions across the GrIS grid cells.

257 Ice with densities above 650 kg·m⁻³ is conventionally classified as cryospheric media,

258 consistent with in situ measurements (Whicker-Clarke et al., 2022). However, because the

259 density-bubble radius relationship for GrIS bare ice remains poorly constrained, we apply a

260 linear density-radius relationship as a first-order approximation for calculating the specific

261 surface area (SSA), where densities of 650 kg·m⁻³ and 916 kg·m⁻³ corresponding to bubble

262 radii of 50 μm and 1500 μm, respectively (Fig. 3a). This parameterization is provisional and

263 awaits future observational validation. For each parameter combination, the band 2 albedo,

264 SSA and the volume fraction of air (V_{air}) were then output by the standalone SNICAR-ADv4.

265 The SSA is a measure of the total surface area of ice-air interfaces relative to the ice mass.

266 The relationship between the SSA (α, units: $m^2 \cdot kg^{-1}$) and ice density and air bubble effective

267 radius is given by Eq.1, where ρ_{blk} is layer bulk ice density used to calculate the volume

268 fraction of air (Eq.2).

269 $$\alpha = \frac{3V_{air}}{\rho_{blk}R_{eff}} \qquad \text{(Eq. 1)}$$

270 $$V_{air} = \frac{\rho_{ice} - \rho_{blk}}{\rho_{ice}} \qquad \text{(Eq. 2)}$$

271 Figure 3b shows the band 2 albedo from the SNICAR-ADv4 lookup table as a function of

272 SSA. This functional degeneracy indicates that the radiative transfer modeling depends

273 primarily on the SSA rather than the specific ice density/bubble size combination.

274 Consequently, the retrieval algorithm selects the (density, radius) combination that most

275 closely reproduces the observed Band 2 albedo. Since MCD43C3 provides the band 2 albedo

276 and SZA for each bare ice grid cell, the corresponding bare ice physical properties can be

277 inferred from the lookup table. It is important to note, however, the resulting bare ice

278 property maps (Figs. 3c-f) represent just one plausible solution among several combinations

279 that could yield similar SSA and albedo values.

280
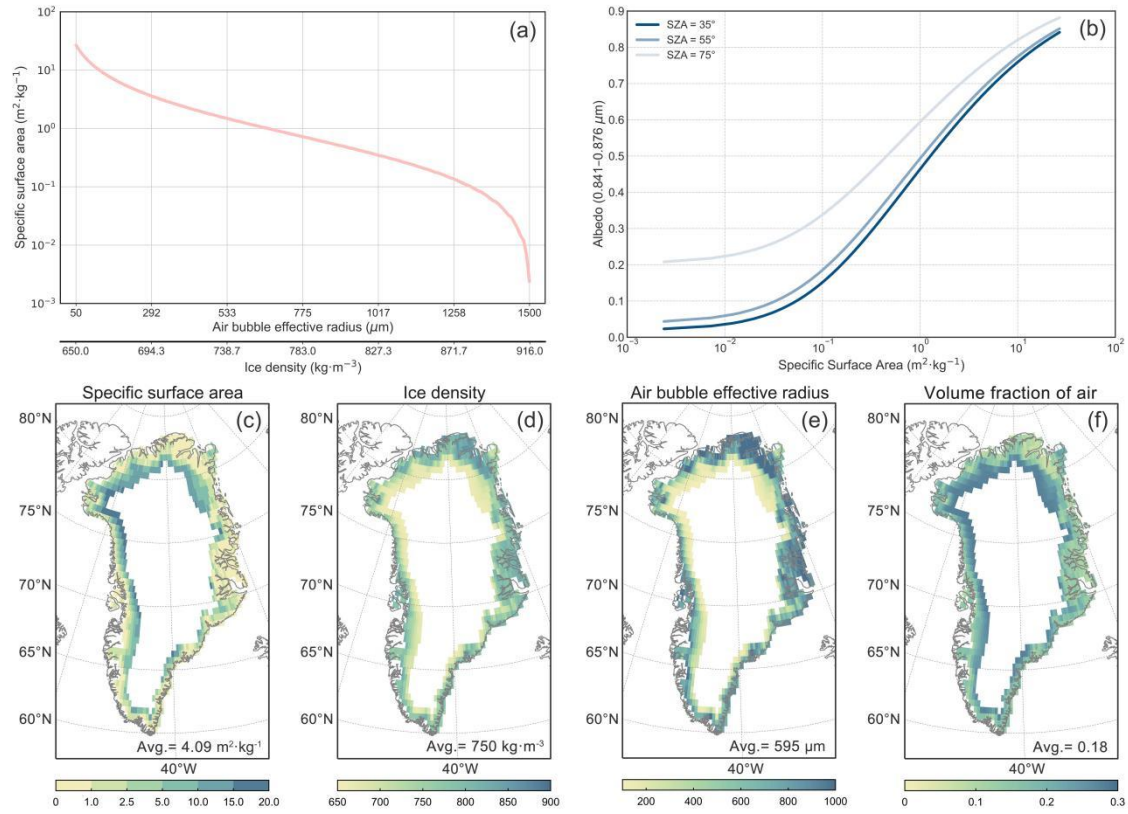
Figure 3. The relationship between ice specific surface area (SSA; $m^2 \cdot kg^{-1}$), air bubble effective radius (μm) and ice density ($kg \cdot m^{-3}$) under a linear density-radius relationship (a first-order approximation) assumed in this study (a). MCD43C3 band 2 (0.841-0.876 μm) albedo as a function of SSA and solar zenith angle (b). Spatial distribution of JJA (c) specific surface area ($m^2 \cdot kg^{-1}$), (d) ice density ($kg \cdot m^{-3}$), (e) air bubble effective radius (μm) and (f) volume fraction of air in the period of 2000-2020.

287

After acquisition of the daily ice density and air bubble effective radius of the GrIS (Figs. R3d and 2e), we again employed the standalone SNICAR-ADv4 model to simulate the NIR and visible albedo for each bare ice grid cell of the GrIS. Using an iterative optimization approach, we derived the equivalent BC concentration by adjusting the BC input parameter in the standalone SNICAR-ADv4 until its simulated visible albedo matched the MODIS MCD43C3 observations. This inversion method relies on the strong influence of LACs on visible albedo and their negligible impact on NIR albedo over bare ice (Schneider et al., 2019). As seen in Figs. 4a-c, there is minimal difference in the albedo in the NIR band, with a slight underestimation of 0.029 by the standalone SNICAR-ADv4. In contrast, the

297   SNICAR-ADv4 significantly overestimated the visible albedo by up to 0.293 when using

298   these bare ice properties, as it did not account for the LACs (Figs. 3d-f). We incrementally

299   adjusted the input BC concentration in the standalone SNICAR model to match the visible

300   albedo values from MCD43C3 data at each GrIS bare ice grid cell (Figs. 4h and i). This

301   process yielded the daily equivalent BC concentrations shown in Fig. 4g. Based on the

302   MODIS data and the standalone SNICAR-ADv4 lookup table, the daily 0.5-deg ice density,

303   air bubble effective radius and equivalent BC data were then processed into monthly

304   timescale as input for CoLM. Besides, it is worth mentioning that not all bare ice grid cells

305   are informed by the bare ice physical properties data in each summer month. These grid cells

306   are filled with the climatological mean values of bare ice physical properties when retrievals

307   fail due to clouds or poor data quality.
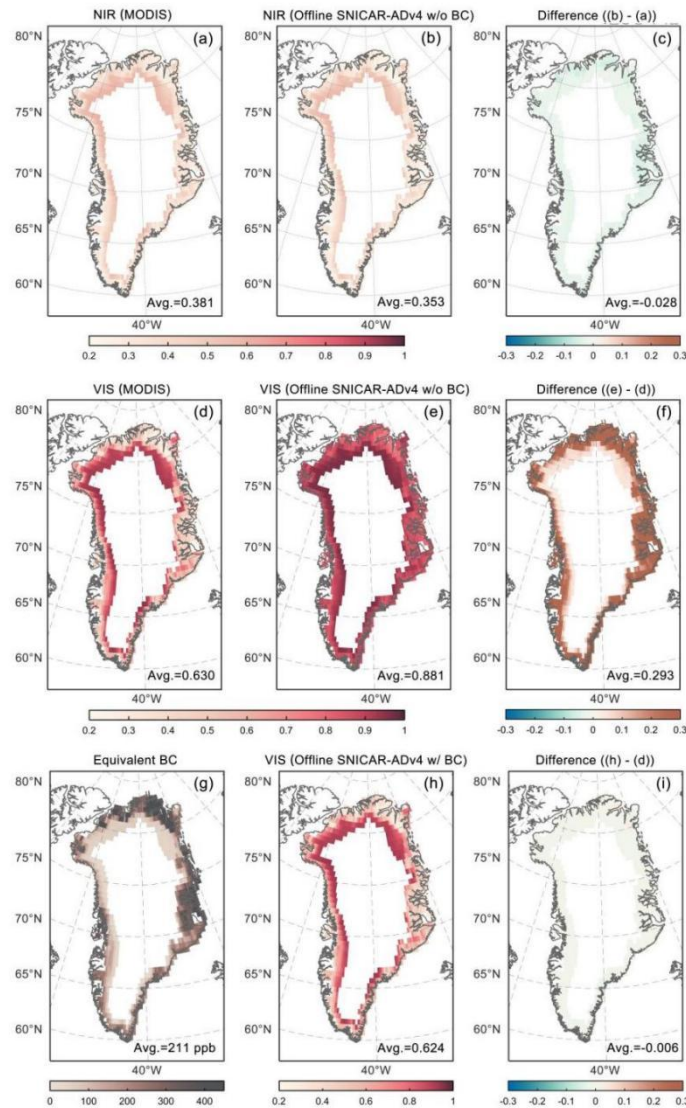
308

Figure 4. The spatial distributions of MODIS bare ice albedo and standalone SNICAR-ADv4 bare ice albedo excluding LACs in (a, b) near-infrared and (c, d) visible bands for the JJA from 2000 to 2020, along with (c, f) their differences. The spatial distributions of (g) equivalent black carbon, (h) the standalone SNICAR-ADv4 bare ice visible albedo with equivalent black carbon (ppb), and (i) its difference from the MODIS bare ice visible albedo.

We use the standalone SNICAR-ADv4 and briefly examine aforementioned factors influencing spectral albedo of ice with direct light conditions, including the SZA, ice density, air bubble effective radius (R_{eff}), and equivalent BC. As shown in Fig. 5a, total internal reflection occurs at wavelengths around 3μm for SZA greater than 55°, and the wavelength range for total internal reflection expands with the increases in SZAs. This phenomenon occurs for pure and smooth ice surfaces but is not representative of naturally occurring ice, which typically has impurities and rough surfaces. For the dependency of albedo on ice density, air bubble effective radius, the spectra show that the albedo declines as the ice density and air bubble radius increases since air bubbles within ice are responsible for the scattering light and smaller bubbles scatter light more efficiently in the visible and near-infrared parts of the spectrum (Figs. 5b-c). Furthermore, BC impacts ice albedo rather uniformly across the visible spectrum and has almost no impact at $\lambda > 1.0$ μm.
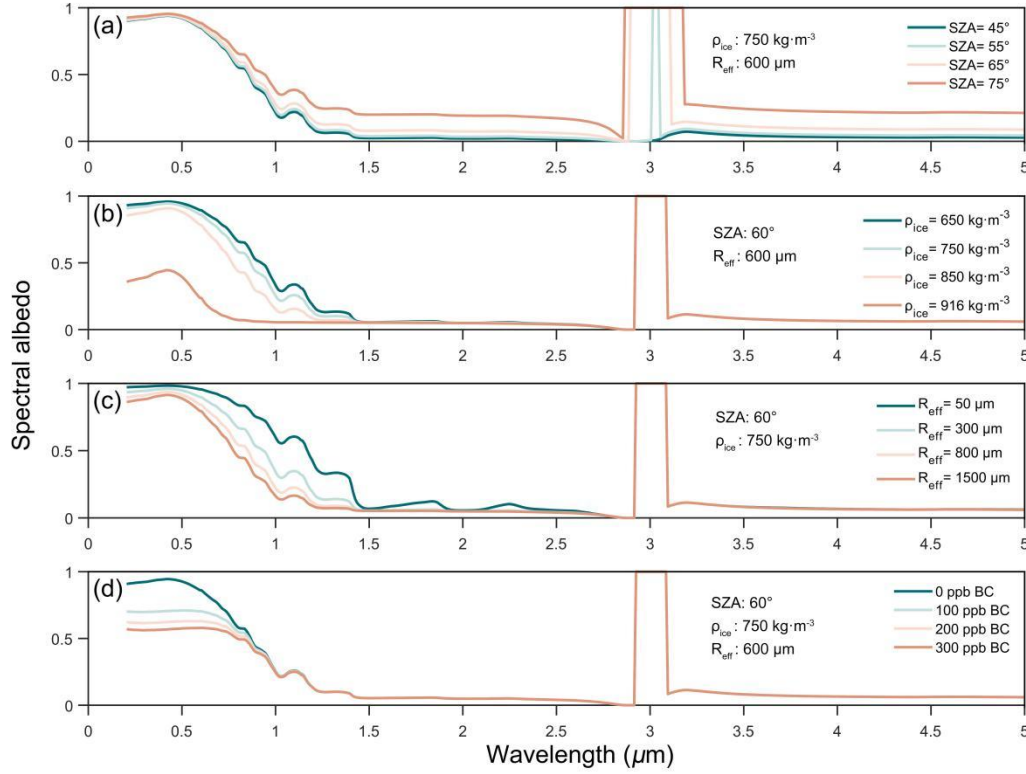
Figure 5. Spectral albedo simulated by standalone SNICAR-ADv4 under direct incident irradiance with varing (a) SZA, (b) ice density, (c) air bubble effective radius and (d) BC concentration.

2.4 Model simulation

We conduct several offline CoLM simulations with the embedded SNICAR-ADv4 and SNICAR-AD schemes on a 0.5×0.5-degree resolution driven by the atmospheric forcing from the 6-hourly European Center for Medium-Range Weather Forecast's fifth-generation atmospheric Reanalysis (ERA5) in the GrIS. Compared with other atmospheric forcings, ERA5's precipitation rates exhibit a higher correlation with measured net accumulation over the GrIS (Schneider et al., 2023). We run the model simulations for the years 1980–2020 and the summer melt season (June, July and August; JJA) during 2000-2020 is used for analysis. Aerosol concentration in the snow layer is calculated based on the prescribed monthly aerosol (BC, dust, OC) wet and dry deposition flux from the CESM2-WACCM simulations participated in CMIP6 experiments (Danabasoglu et al., 2020). The monthly bare ice

343 properties for ice radiative transfer process are inferred from MODIS products using the
344 standalone SNICAR-ADv4 over the bare ice region of the GrIS, covering the JJA from 2000
345 to 2020, as the MODIS products has been available since 2000. To prevent possible unusual
346 model behavior when shifting bare ice albedo schemes, the bare ice properties from the
347 summer of 2000 were used in a brief spin-up run for the variable bare ice conditions in our
348 experimental runs from 1998 to 2000. For land ice patches informed by the ice properties, the
349 bare ice albedo is first calculated and replaces the constant values (0.6 for VIS and 0.4 for
350 NIR). If snow is present over the ice, the new ice albedo of underlying ice column is used as
351 the lower boundary to calculate snow albedo. The total patch albedo is then determined by
352 the fractional coverage of land types and snow cover.

353

354 In this study, we analyzed output variables from three sets of CoLM simulations: (1) those
355 using SNICAR-AD with fixed bare ice albedo (0.6 for visible and 0.4 for near-infrared), (2)
356 those using SNICAR-ADv4 with annually-varying bare ice properties and (3) those using
357 SNICAR-ADv4 with bare ice properties held constant at year 2000 values for all years. The
358 simulations output two variable groups: (a) surface albedo (visible, near-infrared, and
359 shortwave under direct radiation) and bare ice fraction for albedo evaluation; (b) 2-m
360 temperature, snow cover fraction, and snow water equivalent to quantify the effect from the
361 bare ice metamorphism.

362 **3. Results**

363 **3.1 Mapping of GrIS bare ice physical properties**

364 Figures 3b-e display the spatial distribution of summer climatological mean of the bare ice
365 physical properties, including SSA, ice density, air bubble effective radius and volume
366 fraction of air. The bare ice density gradually decreases from the lower-elevation coastal
367 regions toward the interior, while the volume fraction of air show an opposite pattern for it is
368 calculated by bulk ice-air mixture density and pure ice density (Figs. 3c and e). SSA
369 represent the total surface area of ice-air interfaces relative to the mass of ice, determined by
370 the volume fraction of air, effective diameter of air bubbles, and the bulk density of the ice

layer (Whicker-Clarke et al., 2022), with high-value area distributed in the area along the mean equilibrium line (Fig. 3b). Given the large discrepancy in bare ice visible albedo between the standalone SNICAR-ADv4 without LACs and the MCD43C3 in the coastal regions of the GrIS (Figs. 4d and e), higher equivalent BC concentrations occur in these areas compared to inland regions, indicating potentially more severe contamination, particularly in the southeastern and northernmost parts of the GrIS (Fig. 3g)..

3.2 Spatial and Temporal performance of CoLM Simulations

The bare ice region of the GrIS in this study is defined as grid cells with exposed glacier ice (snow cover fraction <100%), where surface albedo is controlled by ice properties but also influenced by residual snow and bare soil patches. Figure 6a shows the spatial distribution of land ice underlying the snowpack. The areas where land ice is the main type of land cover are located in the periphery of the the GrIS with the exception of the southeastern edge. Values of land ice fraction below 1 implies that the corresponding grid cells contain other land cover type, e.g. bare soil. The exposed bare ice fraction (Fig. 6b) is calculated accounting for the snow coverage in each grid cell, utilizing the SNICAR-AD scheme. It is important to note that, despite a slight difference in snow cover fraction simulations, the choice of snow albedo scheme does not affect the selection of bare ice regions. The exposed bare ice fraction frequency distribution is shown in Fig. 6c, in which the bare ice fraction spans from 0 to 0.7, and in most areas, the bare ice fraction is less than 0.5.
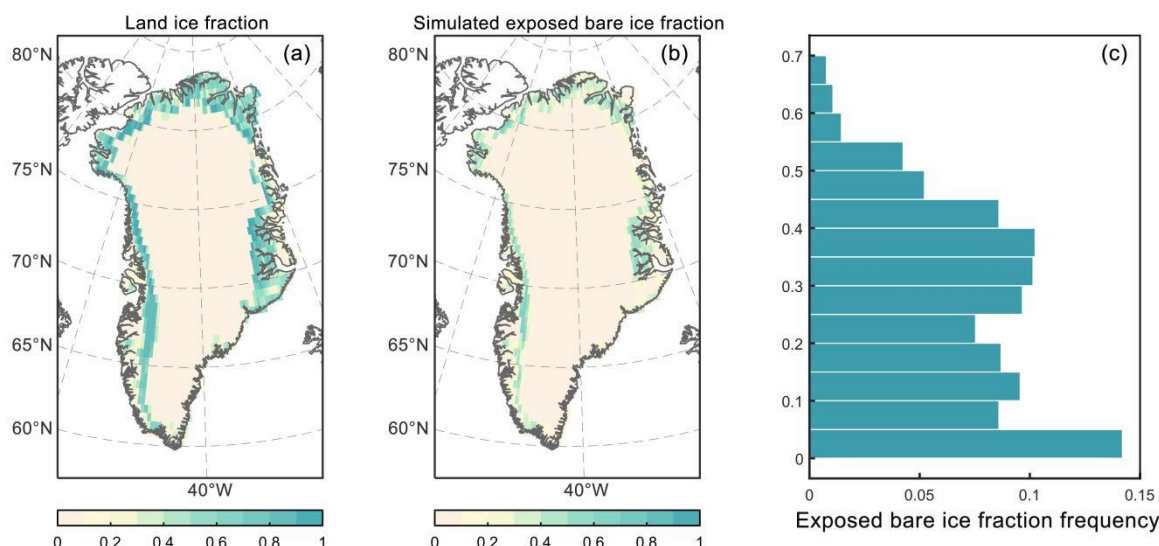
Figure 6. Spatial distribution of (a) the fraction of land ice underlying snowpack and (b) exposed bare ice considering the snow cover simulated by CoLM SNICAR-ADv4 for the JJA from 2000 to 2020. (c) Frequency distribution of exposed bare ice within the bare ice region (excluding grid cells with no exposed bare ice), calculated as the proportion of grid cells within each bare ice fraction interval relative to the total number of bare ice grid cells.

To assess whether the integration of an ice radiative transfer solver in CoLM improves albedo simulations, we compared simulated albedo with the MCD43C3 albedo in shortwave, visible and NIR regions of the spectrum during the summer of 2000-2020 in bare ice region (Fig. 7). Both schemes of SNICAR-AD and SNICAR-ADv4 maintain consistent settings for default snow albedo scheme, with sphere snow grain shape, adding-doubling radiative transfer solver, and BC/dust-snow external mixing state. In other words, the differences in albedo simulated by these two schemes are determined by the treatment for ice albedo. As seen in Figs. 7d-f, it is obvious that the SNICAR-AD enabled CoLM albedo is significantly overestimated across all bare ice region, by 0.086 in shortwave, 0.078 in visible and 0.095 in NIR. Compared with CoLM SNICAR-AD, the application of the SNICAR-ADv4 scheme reduced the overestimation of albedo for all bands, by 38% in the shortwave, 50% in the visible and 28% in the NIR (Figs. 7d-i). Furthermore, comparative analysis of the spatial distributions of correlation coefficients, root mean square errors (RMSE), and linear trends (Figs. S1-S3) reveals that CoLM-SNICAR-ADv4 outperforms CoLM-SNICAR-AD across all evaluation

412 metrics. These metrics were derived from each grid cell by comparing the 21-year summer
413 albedo time series (2000-2020) from model simulations and MODIS observations: correlation
414 coefficients assess temporal agreement, RMSE quantifies deviation magnitudes, and linear
415 trends (obtained via least-squares regression) capture interannual albedo changes. The
416 comprehensive spatial evaluation demonstrates consistent improvements in both the spatial
417 pattern and quantitative representation.

418
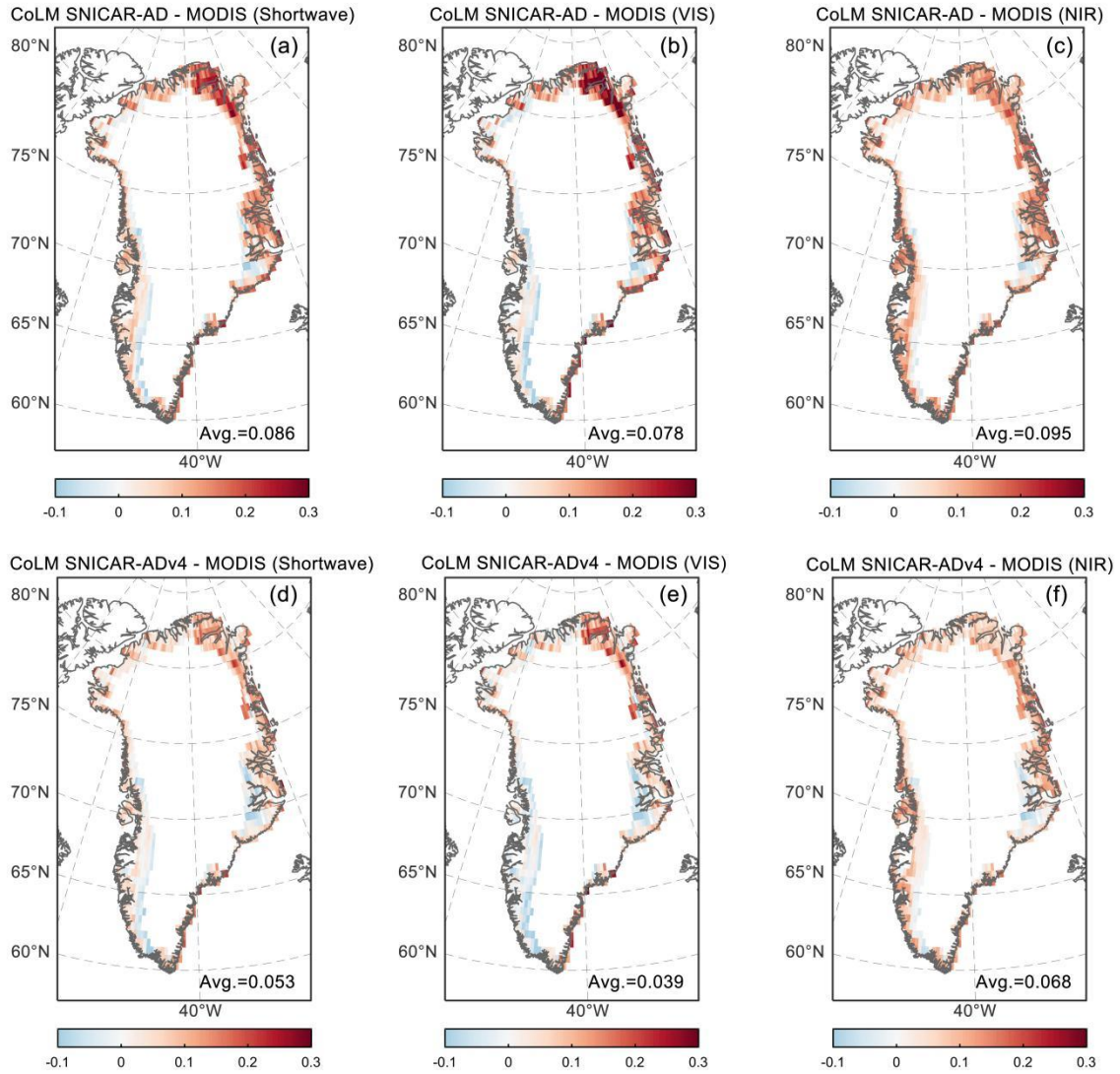
419 **Figure 7.** Spatial distribution of the difference of the 2000-2020 JJA albedo between the
420 CoLM with different snow/ice albedo schemes (SNICAR-AD and SNICAR-ADv4) and the
421 MCD43C3 in the (a, d) shortwave (0.3–5.0 μm), (b, e) visible (0.3–0.7 μm) and (c, f)
422 near-infrared (0.7–5.0 μm) bands.

423

424   The decrease in the positive bias of CoLM SNICAR-ADv4 can also be clearly seen in the

425   shortwave, visible and near-infrared albedo time series, with the area-weighted mean albedo

426   of the GrIS bare ice regions steadily decreasing throughout the summer period from 2000 to

427   2020, compared with CoLM SNICAR-AD (Fig. 8). The albedo of CoLM SNICAR-ADv4

428   fluctuates around 0.47 in the shortwave, 0.53 in the visible, and 0.4 in the NIR, which is

429   approximately 0.05 higher than the corresponding values in MCD43C3. In addition, the

430   CoLM SNICAR-ADv4 simulations exhibit synchronous variations in albedo with those of

431   MCD43C3, and there are relatively high temporal correlations between the CoLM

432   SNICAR-ADv4 and MCD43C4 albedo, with the values up to 0.95 for the shortwave, visible,

433   and NIR bands. In contrast, the albedo from the CoLM SNICAR-AD shows lower correlation

434   with MCD43C3 due to its constant ice albedo treatment. It is obvious that a large interannual

435   variability in the SNICAR-ADv4 enabled CoLM albedo is in consistence with that of the

436   MCD43C3, while the simulated albedo using SNICAR-AD scheme present a weaker

437   interannual variability. Regarding correlation with observations, SNICAR-AD achieves

438   slightly lower correlation (0.91) in the NIR band compared to its performance in the

439   shortwave and visible bands (both 0.92).

440
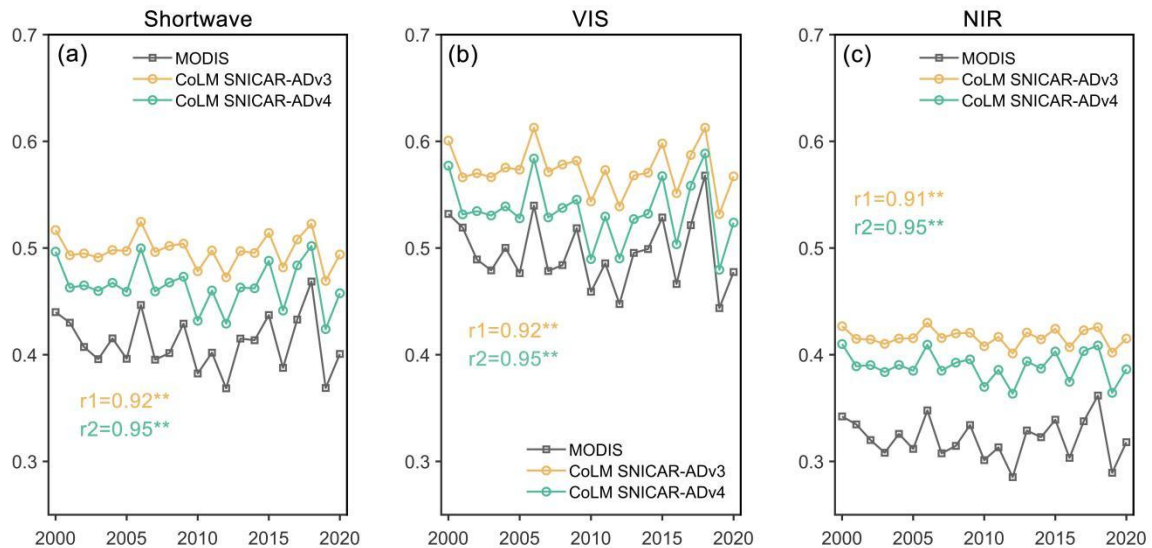
441   **Figure 8.** Time series of the 2000-2020 JJA CoLM SNICAR-AD and SNICAR-ADv4 albedo

442   versus the MCD43C3 albedo over bare ice region, in the (a) shortwave (0.3–5.0 μm), (b)

443   visible (0.3–0.7 μm) and (c) near-infrared (0.7–5.0 μm) bands. Double asterisks indicates

444   significance at the 99% confidence level.

Given that the bias reduction varies across regions with different bare ice coverages, we explore the distribution of the albedo from CoLM SNICAR-AD, CoLM SNICAR-ADv4 and MCD43C3 under different bare ice fractions. Generally, as bare ice fraction increases, CoLM SNICAR-ADv4 can more effectively reduce the overestimation of shortwave broadband albedo (BBA) compared to CoLM SNICAR-AD, due to its improved simulation of bare ice BBA (Fig. 9). For regions where bare ice covers more than half the area, the albedo overestimation of SNICAR-AD was reduced significantly by up to 99%. When the bare ice fraction is between 0.4 and 0.5, the percentage of overestimation reduction in albedo decreases to 74%, followed by regions with bare ice fraction of 0.3-0.4 (52%), 0.2-0.3 (38%), 0.1-0.2 (25%), and 0-0.1 (10%), respectively.
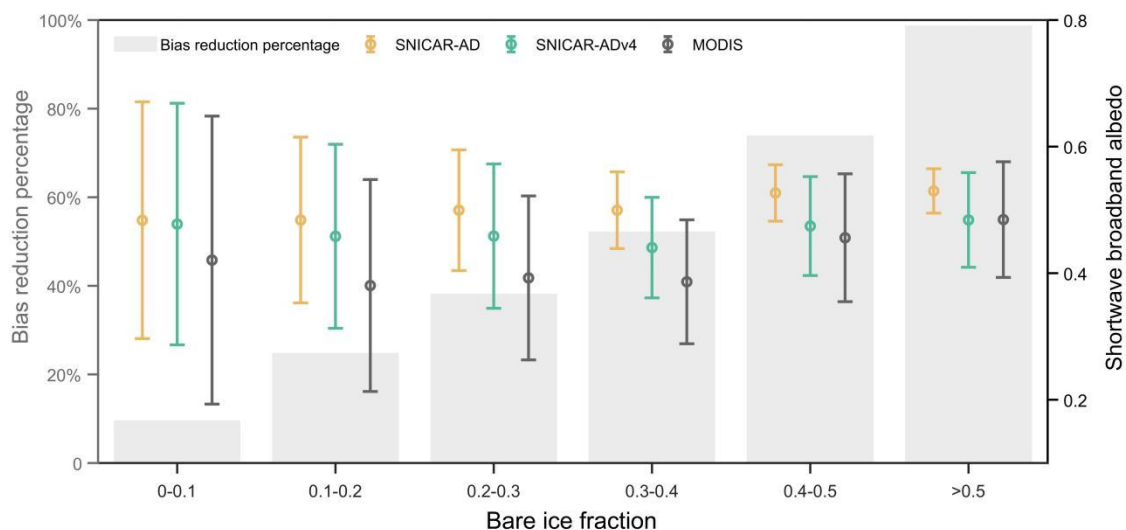
Figure 9. Mean shortwave broadband albedo from CoLM SNICAR-AD, CoLM SNICAR-ADv4 and MCD43C3 under different bare ice fractions (error plots). The uncertainty is calculated as double standard error, which reflects the 95% confidence interval. The percentages of CoLM SNICAR-ADv4 albedo reduction in bias are represented by grey bars.

3.3 A feedback revealed by bare ice properties change

The application of the SNICAR-ADv4 scheme in CoLM has significantly reduced the bias in

albedo simulations. To investigate the regional climatic response to bare ice metamorphism of Greenland's bare ice region, we conduct a simulation in which the bare ice physical properties for each year are set to the values from 2000. By calculating the difference in simulated albedo between the simulations with annually varying bare ice properties and those using the 2000 values, the model sensitivities to the change in summer bare ice albedo can be assessed to quantify its impact on 2-m temperature and snow cover. To better highlight the impact of changes in bare ice physical properties, the study area was restricted to regions with a bare ice fraction larger than 0.4. Figures 10a-c compares the effects of bare ice metamorphism on the 21-year summer mean albedo, 2-m temperature and snow cover fraction, between simulations with annually varying bare ice properties and those using constant year-2000 properties. The regional weighted mean albedo difference between the two experiments reaches 0.032, indicating that the albedo in the bare ice region is reduced by 0.032 during the summer due to bare ice metamorphism (Fig. 10a). This leads to a 0.071°C 2-meter temperature forcing and a -0.011 change in snow cover fraction over the study period (Figs. 10b and c). These results suggest that the temperature increase associated with the change in albedo contributes to snow melting.

Spatially, the regions with strong response of near surface air temperature to bare ice albedo changes are concentrated in the edge of the northwestern and western ablation zone, where the 2-temperature increased by over 0.1°C in most part of these areas (Fig. 10b). A similar response pattern can be also seen in the difference distribution of the snow cover (Fig. 10c), with decrease in snow cover fraction exceeding 0.04 in parts of the northwestern and western GrIS where temperature increases are most pronounced. To further evaluate the hydrological implications of albedo-induced warming, we examined changes in snow water equivalent, which integrates snow accumulation, meltwater retention, and sublimation processes. This analysis indicates that bare ice metamorphism represented by annually varying ice properties leads to a forcing that causes an average snow water equivalent decrease of 1.345 mm (Fig. 10d), consistent with the observed snow cover decline. The statistical distributions of changes in 2-m temperature, snow cover, and snow water equivalent (Fig. 10e) reinforce the finding that certain regions of the GrIS are especially sensitive to reductions in bare ice albedo. These

496   coordinated changes manifest a strong bare ice-albedo feedback in the GrIS bare ice region

497   because bare ice albedo is reduced through physical and biological melt-albedo processes that

498   darken the ice surface as the warming occurs in the ice surface.

499

500   The metamorphism of bare ice could be manifested in the changes in the ice density and air

501   bubble radius with the ice, and these two factors jointly determine the specific surface area

502   (Eq.1) which have one-to-one relationship with the bare ice albedo (Fig. 3b). From Fig. 10f,

503   the difference in BBA shows a strong positive correlation with the specific surface area, with

504   a correlation coefficient of 0.88 (significant at the 99% confidence level), since the two

505   simulations differ solely in their bare ice physical property inputs to the land surface model.

506   As more intense melt processes start in the early summer of the GrIS ablation zone after 2000,

507   the lower specific surface area, linked with the bare ice-albedo feedback, consistently

508   contributes to the reduction of the BBA (Fig. 10f). Additionally, according to the sensitivity

509   of modeled spectral albedo to the relevant parameters of the standalone SNICAR-ADv4

510   model (Fig. 5), the decreased bare ice albedo, associated with a lower specific surface area,

511   suggests an overall increase in ice density and a larger size of air bubbles within the ice in the

512   GrIS bare ice region.

513
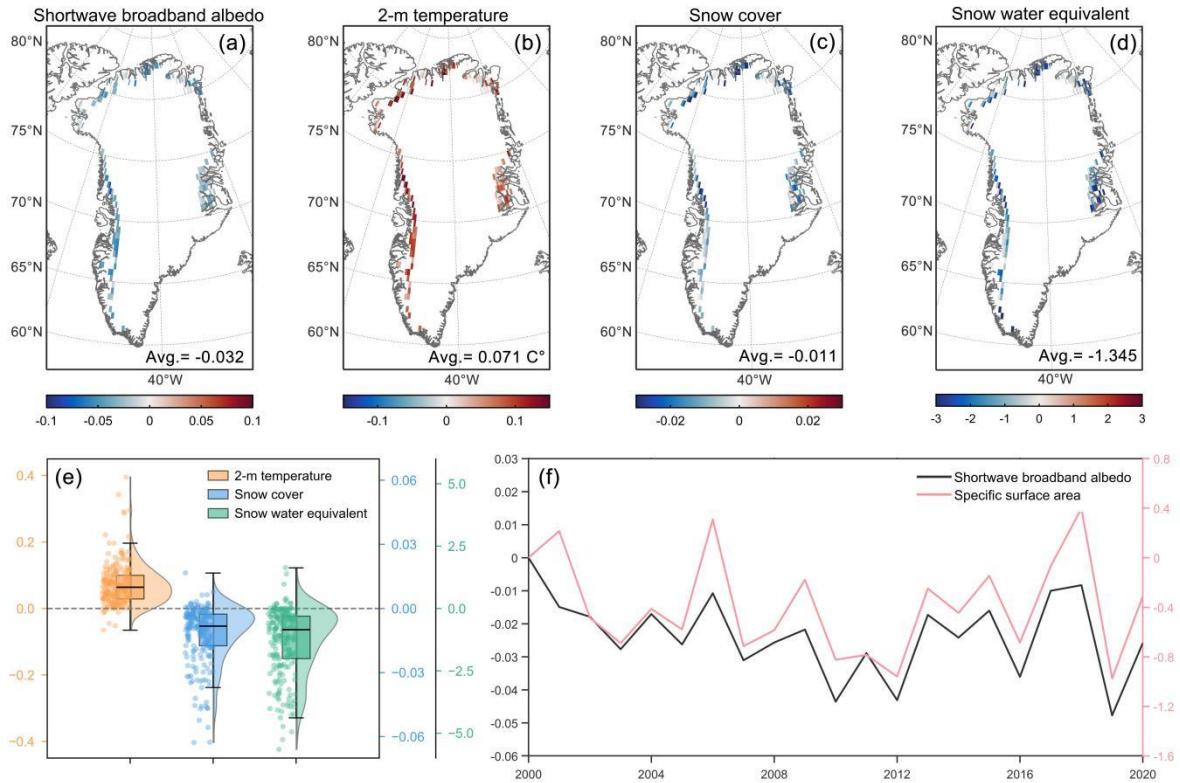
Figure 10. Spatial differences between simulations using annually varying bare ice properties and those using fixed year-2000 values during JJA (June–August) from 2000 to 2020: (a) surface albedo, (b) 2-m air temperature (°C), (c) snow cover fraction, and (d) snow water equivalent. (e) Statistical distributions of differences in 2-m air temperature, snow cover, and snow water equivalent, shown using combined boxplots, left-side jittered points, and right-side half-violin plots. (f) Time series of differences in specific surface area (m²·kg⁻¹) and simulated shortwave broadband albedo between the two experiments.

521

After 2000, the metamorphism of bare ice in the Greenland bare ice region is mainly reflected in the decrease of SSA, which leads to ice darkening. This, in turn, induces regional near-surface temperature increases, causing snowmelt and ultimately resulting in a reduction of snow cover. Changes in snow cover directly determine the extent of bare ice exposure and significantly affect the albedo through snow-albedo feedback. The obvious snow cover contraction attributed to the changes in the physical properties of bare ice will cause more dark ice exposure and darkening, and make a constant contribution to albedo reduction in this ablation zone, suggesting a potential linkage between the bare ice-albedo and the

530 snow-albedo feedback.

531

4. Conclusions and Discussion

533 In this study, we incorporated SNICAR-ADv4 into the CoLM and made an enhanced

534 MODIS-informed bare ice physical properties to explore the response of the bare ice albedo

535 to the ice metamorphism under polar warming. The use of SNICAR-ADv4 in CoLM

536 significantly reduces the severe overestimation originated from the default ice albedo

537 treatment, with the improvement of the albedo modeling by 38%, 50% and 28% for the BBA,

538 visible and NIR albedo. The snow and ice treatment used in CoLM SNICAR-ADv4 schemes,

539 and SNICAR-AD are summarized in the Fig. 1, and it is evident that SNICAR-ADv4

540 performs radiative transfer calculations not only over the snow column but also over the ice

541 column. During the summertime of 2000-2020, the bare ice BBA decreased by 0.032 due to

542 the changes in bare ice physical properties. The subsequent darkening of the bare ice led to a

543 2-m air temperature forcing of 0.071°C, a change in snow cover of -0.011 and snow water

544 equivalent of -1.345 mm over the 21-year period, suggesting that even a slight reduction in

545 bare ice albedo can produce noticeable climate responses in ablation region.

546

547 Our results are consistent with, and extend, recent progress in modeling bare ice albedo

548 modeling over the GrIS. Antwerpen et al. (2022) demonstrated that the regional MAR model

549 overestimated bare ice albedo by 22.8% below 70°N, leading to significant underestimation

550 of meltwater production. Similarly, Wicker-Clarke et al. (2024) found that the global

551 ELM-E3SM model overestimated shortwave broadband albedo by ~5% due to the use of

552 fixed albedo parameters, and showed that incorporating more realistic bare ice albedo

553 reduced the surface mass balance by approximately 145 Gt between 2000 and 2021.

554 Although both studies focus on the GrIS, they differ in model structure and spatial resolution:

555 MAR is a high-resolution regional climate model, while ELM-E3SM is part of a

556 coarser-resolution global Earth system model. Despite these differences, both studies

557 highlight a persistent bias-systematic overestimation of bare ice albedo. The convergence of

558 evidence from diverse modeling frameworks underscores the need to improve bare ice

representation in land surface models. Building on these insights, our study examines the role of bare ice metamorphism, particularly changes in specific surface area, in driving progressive surface darkening. By isolating the feedback between evolving ice properties and surface energy balance, we propose a physically mechanism for the observed albedo decline. Our sensitivity analysis underscores how bare ice metamorphism can influence surface energy balance and the importance of incorporating such processes in future model developments.

Our findings also highlight the role of the bare ice-albedo feedback linked to changes in ice surface properties, as shown in Fig. 11. A marked reduction in snow cover occurred due to lowered albedo in the ablation zone, exposing more bare ice and further reducing regional albedo, especially in northern GrIS. This agrees with previous findings that increased bare ice exposure has intensified the snow-albedo feedback in this region, with its strength rising by 51% from 2001 to 2017 (Ryan et al., 2019). The physical processes governing snowpack evolution play a crucial role in modulating surface albedo and associated feedbacks, particularly in the ablation zone of the GrIS, where snow loss accelerates bare ice exposure and amplifies radiative forcing. More specifically, new snow quickly loses reflectivity through grain growth and vapor diffusion, with subsequent changes driven by temperature gradients and compaction (Flanner and Zender, 2006). Meltwater accelerates these processes through melt-refreeze cycles (Brun 1989), creating a self-reinforcing system where both ice exposure and snow aging enhance surface darkening. While biological and hydrological factors such as algal growth play a secondary role in ice darkening (Ryan et al., 2019), our results demonstrate that changes in bare ice properties, particularly a downward trend in specific surface area at a rate of -0.007 yr^{-1}, exert significant control over meltwater production. We collectively term these processes of the variation in the bare ice albedo associated with snow melting the bare ice-snow-albedo feedback (Fig. 11). As rising temperatures may further reduce ice albedo, this feedback could substantially increase Greenland's contribution to sea level rise through enhanced melting (Ryan et al., 2019), highlighting the need for improved process understanding in climate projections.

589   This study advances our understanding of the performances of the GrIS's snow and ice

590   albedo simulations using different snow/ice schemes (SNICAR-AD and SNCIAR-ADv4),

591   and the amplifying effect of bare ice on the albedo reduction through bare ice-snow-feedback

592   mechanism. However, three key limitations constrain our current findings. First, the

593    $0.5° \times 0.5°$ resolution is insufficient to accurately represent the narrow ablation zone, and big

594   resolution gap between MODIS data and the model output is a limitation of this study.

595   Second, CoLM's representation of GrIS glaciers prescribed fixed ice thickness and mass with

596   internally retained meltwater prevents calculation of surface mass balance, and excludes ice

597   melt contributions to runoff. Although computationally efficient, this simplification

598   systematically underestimates meltwater export from Greenland's ablation zones, where ice

599   dynamical processes dominate mass loss. Third, methodological constraints prevent

600   independent quantification of ice density and air bubble size effects, as their relationship is

601   prescribed in the lookup table (ρ_{ice}=650 kg·m^{-3} corresponds to R_{eff}=100 μm, ρ_{ice}=916 kg·m^{-3}

602   corresponds to R_{eff}=1500 μm) based on the standalone SNICAR-ADv4 model. Future work

603   will address these limitations by employing higher-resolution modeling for more precise

604   delineation of bare ice margins, coupling a dynamic ice sheet model to properly simulate the

605   SMB and ice-melt runoff contributions, and establishing observational constraints on ice

606   density and air bubble effective radius evolution to improve ice albedo modeling. Future

607   efforts are also needed to consider the actual LACs concentrations within the ice, including

608   BC, dust and snow algae, rather than relying on equivalent BC, and evaluate their impacts on

609   GrIS mass loss using fully coupled land-atmosphere models, which may reveal more

610   pronounced feedbacks than offline simulations.

611

612
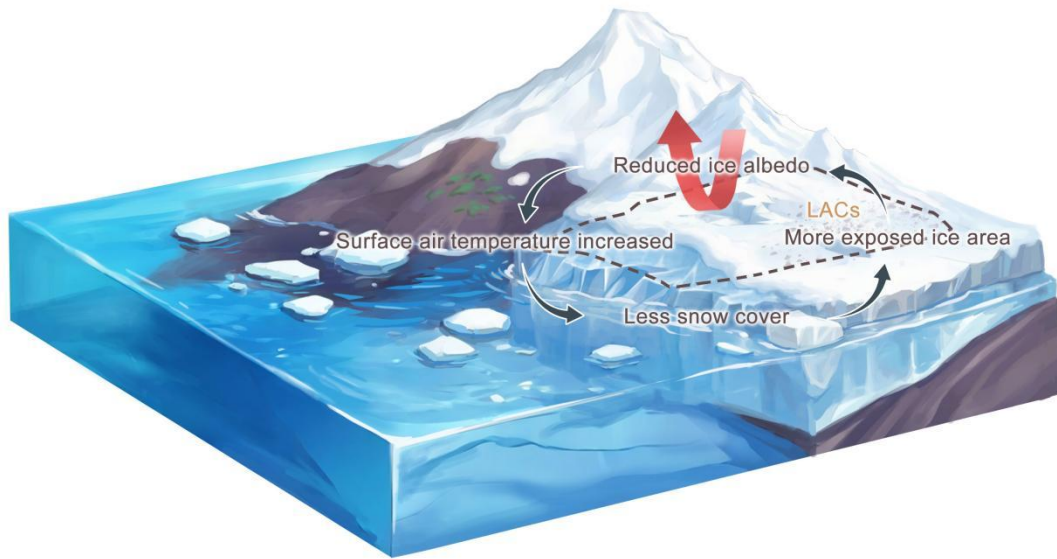
Figure 11. Illustration of the bare ice-snow-albedo feedback over the Greenland Ice Sheet. A reduction in ice albedo, primarily driven by changes in bare ice surface properties, exposes more bare ice, further lowering regional albedo and raising surface air temperatures. This leads to a decline in snow cover, which accelerates bare ice exposure and reinforces radiative forcing. This positive feedback loop intensifies melt, particularly in the ablation zone, contributing to increased surface darkening and meltwater production.

Data availability. The SNICAR-ADv4 enabled CoLM2024 code is available on GitHub at https://github.com/guoshuyang23/CoLM-SNICARADv4. The standalone SNICAR-ADv4 used in this study can be downloaded at https://github.com/chloewhicker/SNICAR-ADv4. MODIS snow cover data (MOD10C1) used to make the cloud and snow mask for bare ice pixels is available at https://nsidc.org/data/mod10c1/versions/6. MODIS surface reflectance data (MOD09CMG) used to retrieve the bare ice properties is from https://doi.org/10.5067/MODIS/MOD09CMG.061. MODIS surface albedo data (MCD43C3) used to evaluate the simulations and retrieve the bare ice properties is from https://doi.org/10.5067/MODIS/MCD43C3.061

Author contributions. SYG designed the study and wrote the paper. YJD was responsible for to conceptualization, supervision, and funding acquisition. HY contributed to revisions of the

632   manuscript. HBL provided technical support.

633

634   *Competing interests*. The contact author has declared that neither they nor their co-authors

635   have any competing interests.

636

637   *Acknowledgements*. We thank Chloe A. Whicker-Clarke for sharing the method for

638   processing ice optical property files in the standalone SNICAR-ADv4 for use in land surface

639   models.

640

641   *Financial support*. This research was funded by the Guangdong Major Project of Basic and

642   Applied Basic Research (2021B0301030007), the Natural Science Foundation of China

643   (under Grants U2342227, 42075160, and 42088101), the Southern Marine Science and

644   Engineering Guangdong Laboratory (Zhuhai) (No. SML2023SP216), and the specific

645   research fund of the Innovation Platform for Academicians of Hainan Province

646   (YSPTZX202143).

647

References

Abolafia-Rosenzweig, R., He, C., McKenzie Skiles, S., Chen, F., and Gochis, D.: Evaluation and optimization of snow albedo scheme in Noah-MP land surface model using in situ spectral observations in the Colorado Rockies, J. Adv. Model. Earth Syst., 14, e2022MS003141, https://doi. org/10.1029/2022MS003141, 2022.

Alexander, P. M., Tedesco, M., Fettweis, X., van de Wal, R. S. W., Smeets, C. J. P. P., and van den Broeke, M. R.: Assessing spatio-temporal variability and trends in modelled and measured Greenland ice sheet albedo (2000–2013), The Cryosphere, 8(6), 2293–2312, https://doi.org/10. 5194/tc-8-2293-2014, 2014.

Antwerpen, R., Tedesco, M., Fettweis, X., Alexander, P.,and vandeBerg, W. J.: Assessing bare-ice albedo simulated byMAR overthe Greenland icesheet(2000–2021) andimplications formeltwater production estimates, The Cryosphere, 16(10), 4185–4199, https://doi.org/10. 5194/tc-16-4185-2022, 2022.

Box, J. E., Fettweis, X., Stroeve, J. C., Tedesco, M., Hall, D. K., and Steffen, K.: Greenland ice sheet albedo feedback: Thermodynamics and atmospheric drivers, The Cryosphere, 6(4), 821–839, https://doi.org/10.5194/tc-6-821-2012, 2012.

Briegleb, B. P. and Light, B.: A Delta-Eddington multiple scattering parameterization for solar radiation in the sea ice component of the Community Climate System Model, NCAR/TN472+STR, National Center for Atmospheric Research, 108 pp., https://doi.org/10.5065/D6B27S71, 2007.

Brun, E.: Investigation of wet-snow metamorphism in respect of liquid-water content, Ann. Glaciol., 13, 22－26, https://doi.org/10.3189/S0260305500007635, 1989.

Chen, X., Zhang, X. , Church, J. A., Watson, C. S., King, M. A., Monselesan, D., Legresy, B., and Harig C.: The increasing rate of global mean sea-level rise during 1993-2014, Nat. Clim. Change,7, 492–495, https://doi.org/10.1038/nclimate3325, 2017.

Chevrollier, L. A., Cook, J. M., Halbach, L., Jakobsen, H., Benning, L. G., Anesio, A. M., and Tranter, M.: Light absorption and albedo reduction by pigmented microalgae on

675   snow and ice, J. Glaciol., 69(274), 333–341. https://doi.org/10.1017/jog.2022.64, 2023.

676   Cogley, J. G., Hock, R., Rasmussen, L. A., Arendt, A. A., Bauder, A., Braithwaite, R. J.,
677   Jansson, P., Kaser, G., Möller, M., Nicholson, L.: Glossary of glacier mass balance and
678   related terms (p. 86), IHP-VII Technical Documents in Hydrology No, 2011.

679   Cook, J. M., Tedstone, A. J., Williamson, C., McCutcheon, J., Hodson, A. J., Dayal, A.,
680   Skiles, M., Hofer, S., Bryant, R., McAree, O., McGonigle, A., Ryan, J., Anesio, A. M.,
681   Irvine-Fynn, T. D. L., Hubbard, A., Hanna, E., Flanner, M., Mayanna, S., Benning, L. G.,
682   van As, D., Yallop, M., McQuaid, J. B., Gribbin, T., and Tranter, M.: Glacier algae
683   accelerate melt rates on the south-western Greenland Ice Sheet, The Cryosphere, 14,
684   309330, https://doi.org/10.5194/tc-14-309-2020, 2020.

685   Danabasoglu, G., Lamarque, J. F., Bacmeister, J., Bailey, D. A., DuVivier, A. K., Edwards, J.,
686   Emmons, L. K., Fasullo, J. T., Garcia, R., Gettelman, A., Hannay, C., Holland, M. M.,
687   Large, W. G., Lauritzen, P., Lawrence, D. M., Lenaerts-Jan T. M., Lindsay, K.,
688   Lipscomb, W. H, Mills, M. J., Neale, R., Oleson, K., Otto-Bliesner, B., Phillips, A. S.,
689   Sacks, W. J., Tilmes, S., van Kampenhout, L., Vertenstein, M., Bertini, A., Dennis, J.,
690   Deser, C., Fischer, C., Fox-Kemper, B., Elizabeth-Kay, J., Kinnison, D., Kushner, P.,
691   Larson, V. E., Long, M., Mickelson, S., Moore, J. K., Nienhouse, E., Polvani, L., Rasch,
692   P. J., and Strand, W. G..: The community Earth system model version 2 (CESM2), J.
693   Adv. Model. Earth Syst., 12, https://doi.org/10.1029/2019MS001916, 2020.

694   Dang, C., Zender, C. S., and Flanner, M. G.: Intercomparison and improvement of
695   two-stream shortwave radiative transfer schemes in Earth system models for a unified
696   treatment of cryospheric surfaces, The Cryosphere, 13(9), 2325–2343.
697   https://doi.org/10.5194/tc-13-2325-2019, 2019.

698   Feng, S., Cook, J. M., Naegeli, K., Anesio, A. M., Benning, L. G., and Tranter, M.: The
699   impact of bare ice duration and geo-topographical factors on the darkening of the
700   Greenland Ice Sheet, Geophys. Res. Lett., 51, e2023GL104894, https://doi.
701   org/10.1029/2023GL104894, 2024.

702   Flanner, M. G., and Zender, C. S. Linking snowpack microphysics and albedo evolution, J.

Geophys. Res., 111(D12), https://doi.org/10.1029/2005JD006834, 2006.

Flanner, M. G., Arnheim, J. B., Cook, J. M., Dang, C., He, C., Huang, X., Singh, D., Skiles, S. M., Whicker, C. A., and Zender, C. S.: SNICAR-ADv3: a community tool for modeling spectral snow albedo, Geosci. Model Dev., 14, 7673 – 7704, https://doi.org/10.5194/gmd-14-7673-2021, 2021.

Flanner, M. G., Liu, X., Zhou, C., Penner, J. E., and Jiao, C.: Enhanced solar energy absorption by internally-mixed black carbon in snow grains, Atmos. Chem. Phys., 12(10), 4699–4721, https://doi.org/10.5194/acp-12-4699-2012, 2012.

Flanner, M. G., Zender, C. S., Randerson, J. T., and Rasch, P. J.: Present-day climate forcing and response from black carbon in snow. J. Geophys. Res., 112(D11). https://doi.org/10.1029/2006jd008003, 2007.

Friedl, M.A., Sulla-Menashe, D., Tan, B., Schneider, A., Ramankutty, N., Sibley, A., and Huang X.: Modis collection 5 global land cover: algorithm refinements and characterization of new datasets. Remote Sens. Environ, 114(1), 168–182, https://doi.org/10.1016/j.rse.2009.08.016, 2010

Gardner, A. S., and Sharp, M. J.: A review of snow and ice albedo and the development of a new physically based broadband albedo parameterization, J. Geophys. Res., 115(F1), F01009, https://doi.org/10.1029/2009JF001444, 2010.

Hao, D., Bisht, G., Rittger, K., Bair, E., He, C., Huang, H., Dang, C., Stillinger, T., Gu., Y., Wang, H., Qian, Y., Leung, L. R.: Improving snow albedo modeling in the E3SM land model (version 2.0) and assessing its impacts on snow and surface fluxes over the Tibetan Plateau, Geosci. Model Dev., 16(1), 75–94, https://doi.org/10.5194/gmd-16-75-2023, 2023.

He, C., and Flanner, M.: Snow albedo and radiative transfer: Theory, modeling, and parameterization. In Springer series in light scattering (pp. 67–133), Springer, 2020.

He, C., Flanner, M. G., Chen, F., Bariage, M., Liou, K. N., Kang, S., Ming, J., and Qian, Y.: Black carbon-induced snow albedo reduction over the Tibetan Plateau: Uncertainties

from snow grain shape and aerosol–snow mixing state based on an updated SNICAR model, Atmos. Chem. Phys., 18, 11507–11527, https://doi.org/10.5194/ACP-18-11507-2018, 2018.

He, C., Flanner, M., Lawrence, D. M., and Gu, Y.: New features and enhancements in community land model (CLM5) snow albedo modeling: Description, sensitivity, and evaluation, J. Adv. Model. Earth Syst., 16, e2023MS003861, https://doi.org/10.1029/2023MS003861, 2024.

He, C., Liou, K. N., Takano, Y., Chen, F., and Barlage, M.: Enhanced snow absorption and albedo reduction by dust-snow internal mixing: Modeling and parameterization, J. Adv. Model. Earth Syst., 11(11), 3755–3776, https://doi.org/10.1029/2019ms001737, 2019.

He, C., Takano, Y., Liou, K. N., Yang, P., Li, Q., and Chen, F.: Impact of snow grain shape and black carbon–snow internal mixing on snow optical properties: Parameterizations for climate models, Journal of Climate, 30(24), 10019–10036, https://doi.org/10.1175/jcli-d-17-0300.1, 2017.

Hofer, S., Tedstone, A. J., Fettweis, X. and Bamber, J. L.: Decreasing cloud cover drives the recent mass loss on the Greenland Ice Sheet, Sci. Adv., 3, e1700584, https://doi.org/10.1126/sciadv.1700584, 2017.

King, M. D., Howat, I. M., Candela, S. G., Noh, M. J., Jeong, S., Noël, B. P. Y., Van den Broeke, M. R., Wouters, B., and Negrete, A.: Dynamic ice loss from the Greenland Ice Sheet driven by sustained glacier retreat, Commun. Earth Environ., 1(1), 1. https://doi.org/10.1038/s43247-020-0001-2, 2020.

Kochtitzky, W., Copland, L., King, M., Hugonnet, R., Jiskoot, H., Morlighem, M., Millan, R., Khan, S. A., and Noël, B.: Closing Greenland's mass balance: Frontal ablation of every Greenlandic glacier from 2000 to 2020, Geophys. Res. Lett., 50, e2023GL104095, https://doi. org/10.1029/2023GL104095, 2023.

Li, Y., Yang, K., Gao, S., Smith, L.C., Fettweis, X., and Li, M.: Surface meltwater runoff routing through a coupled supraglacial-proglacial drainage system, Inglefield Land, northwest Greenland, Int. J. Appl. Earth. Obs, Geoinf, p. 106.

758   https://doi.org/10.1016/j.jprocont.2022.08.003, 2022.

759   Mouginot, J., Rignot, E., Bjørk, A. A., van den Broeke, M., Millan, R., Morlighem, M., Noël,

760   B., Scheuchl, B., and Wood, M.: Forty-six years of Greenland Ice Sheet mass balance

761   from 1972 to 2018, P. Natl. Acad. Sci., 116, 9239–9244,

762   https://doi.org/10.1073/pnas.1904242116, 2019.

763   Mullen, P. C., and Warren, S. G.:. Theory of the optical properties of lake ice, J. Geophys.

764   Res., 93(D7), 8403–8414, https:// doi.org/10.1029/JD093iD07p08403, 1988.

765   Naegeli, K., Damm, A., Huss, M., Wulf, H., Schaepman, M., and Hoelzle, M.:

766   Cross-Comparison of albedo products for glacier surfaces derived from airborne and

767   satellite (Sentinel-2 and Landsat 8) optical data, Remote Sens., 9(2), 110.

768   https://doi.org/10.3390/ rs9020110, 2017.

769   Nolin, A.W., and Stroeve, J.: The changing albedo of the Greenland ice sheet: implications

770   for climate modeling, Ann. Glaciol., 25, 51–57. https://doi.

771   org/10.1017/s0260305500013793, 1997.

772   Picard, G., Libois, Q., and Arnaud, L.: Refinement of the ice ab-sorption spectrum in the

773   visible using radiance profile measurements in Antarctic snow, The Cryosphere, 10(6),

774   2655–2672, https://doi.org/10.5194/tc-10-2655-2016, 2016

775   Ryan, J. C.: Contribution of surface and cloud radiative feedbacks to Greenland Ice Sheet

776   meltwater production during 2002-2023, Commun. Earth Environ., 5(538),

777   https://doi.org/10.1038/s43247-024-01714-y, 2024.

778   Ryan, J. C., Smith, L. C., van As, D., Cooley, S. W., Cooper, M. G., Pitcher, L. H., and

779   Hubbard, A.: Greenland Ice Sheet surface melt amplified by snowline migration and

780   bare ice exposure, Sci. Adv., 5(3), eaav3738, https://doi.org/10.1126/sciadv.aav3738,

781   2019.

782   Sasgen, I., Wouters, B., Gardner, A.S., King, M.D., Tedesco, M., Landerer, F.W., Dahle, C.,

783   Save, H., and Fettweis, X.: Return to rapid ice loss in Greenland and record loss in 2019

784   detected by the GRACE-FO satellites, Commun. Earth Environ, 1, 1-8.

https://doi.org/10.1038/s43247-020-0010-1, 2020.

Schaaf, C., Wang, Z., and Strahler, A. H.: Commentary on Wang and Zender-MODIS snow albedo bias at high solar zenith angles relative to theory and to in situ observations in Greenland, Remote. Sens. Environ., 115, 1296 − 1300, https://doi.org/10.1016/j.rse.2011.01.002, 2011.

Schaaf, C., and Wang, Z.: MODIS/Terra+Aqua BRDF/Albedo Albedo Daily L3 Global 0.05Deg CMG V061 [Dataset]. NASA EOSDIS Land Processes DAAC, https://doi.org/10.5067/MODIS/MCD43C3.06, 2021.1

Schneider, A., Flanner, M., De Roo, R., and Adolph, A.: Monitoring of snow surface near-infrared bidirectional reflectance factors with added light-absorbing particles. The Cryosphere, 13(6), 1753–1766, https://doi.org/10.5194/tc-13-1753-2019, 2019

Schneider, A., Zender, C., Loeb, N., and Price, S.: Useofshallow icecoremeasurements toevaluate andconstrain 1980–1990 global reanalyses oficesheetprecipitation rates. Geophys. Res. Lett., 50(19), e2023GL103943, https://doi.org/10.1029/2023GL103943, 2023

Shimada, R., Takeuchi, N., and Aoki, T.: Inter-annual and geographical variations in the extent of bare ice and dark ice on the Greenland ice sheet derived from MODIS satellite images, Front Earth Sci., 4, 43, https://doi.org/10.3389/feart.2016.00043, 2016.

Stibal, M., Box, J. E., Cameron, K. A., Langen, P. L., Yallop, M. L., Mottram, R. H., Khan, A. L., Molotch, N. P., Chrismas, N. A. M., Quaglia, F. C., Remias, D., Smeets, P., Van den Broeke, M. R., and Ryan, J.: Algae drive enhanced darkening of bare ice on the Greenland ice sheet, Geophys. Res. Lett., 44(22), 11463–11471, https://doi.org/10.1002/2017GL075958, 2017.

Stroeve, J., Box, J. E., Gao, F., Liang, S., Nolin, A., and Schaaf, C.: Accuracy assessment of the MODIS 16-day albedo product for snow: Comparisons with Greenland in situ measurements, Remote. Sens. Environ., 94(1), 46–60. https://doi.org/10.1016/j.rse.2004.09.001, 2005.

812   Tedesco, M., Doherty, S., Fettweis, X., Alexander, P., Jeyaratnam, J., and Stroeve, J.: The

813   darkening of the Greenland ice sheet: Trends, drivers, and projections (1981–2100), The

814   Cryosphere, 10(2), 477–496, https://doi.org/10.5194/tc-10-477-2016, 2016.

815   Tedstone, A. J., Cook, J. M., Williamson, C. J., Hofer, S., McCutcheon, J., Irvine-Fynn, T.,

816   Gribbin, T., and Tranter, M.: Algal growth and weathering crust state drive variability in

817   western Greenland Ice Sheet ice albedo, The Cryosphere, 14, 521–538,

818   https://doi.org/10.5194/tc-14-521-2020, 2020.

819   Tedstone, A. J., Bamber, J. L., Cook, J. M., Williamson, C. J., Fettweis, X., Hodson, A. J.,

820   and Tranter, M.: Dark ice dynamics of the south-west Greenland Ice Sheet, The

821   Cryosphere, 11, 24912506, https://doi.org/10.5194/tc-11-2491-2017, 2017.

822   Toon, O. B., McKay, C. P., Ackerman, T. P., and Santhanam, K.: Rapid calculation of

823   radiative heating rates and photodissocia-tion rates in inhomogeneous multiple

824   scattering atmospheres, J. Geophys. Res., 94(D13), 16287–16301,

825   https://doi.org/10.1029/ jd094id13p16287, 1989.

826   Urraca, R., Lanconelli, C., and Cappucci, F.: Gobron, N. Comparison of Long-Term Albedo

827   Products against Spatially Representative Stations over Snow, Remote Sens., 14, 3745.

828   https://doi.org/ 10.3390/rs14153745, 2022.

829   van den Broeke, Box, J., Fettweis, X., Hanna, E., Noël, B., Tedesco, M., van As, D., van de

830   Berg, W. J., and van Kampenhout, L.: Greenland Ice Sheet Surface Mass Loss: Recent

831   Developments in Observation and Modeling, Curr. Clim. Change Rep., 3, 345356,

832   https://doi.org/10.1007/s40641-017-0084-8, 2017.

833   Vermote, E.: MODIS/Terra Surface Reflectance Daily L3 Global 0.05Deg CMG V061 [Data

834   set]. NASA EOSDIS Land Processes Distributed Active Archive Center,

835   https://doi.org/10.5067/MODIS/MOD09CMG.061. 2021.

836   Warren, S. G., and Wiscombe, W. J.:. A model for the spectral albedo of snow. II: Snow

837   containing atmospheric aerosols, J. Atmos. Sci., 37(12), 2734–2745,

838   https://doi.org/10.1175/1520-0469(1980)037<2734:amftsa>2.0.co;2, 1980.

839 Whicker-Clarke, A., Antwerpen, R., Flanner, M. G., Schneider, A., Tedesco, M., and Zender,

840   C. S.: The effect of physically based ice radiative processes on Greenland ice sheet

841   albedo and surface mass balance in E3SM, J. Geophys. Res.-Atmos., 129,

842   e2023JD040241, https://doi.org/10.1029/ 2023JD040241, 2024.

843 Whicker-Clarke, A., Flanner, M. G., Dang, C., Zender, C. S., Cook, J. M., and Gardner, A. S.:

844   SNICAR-ADv4: A physically based radiative transfer model to represent the spectral

845   albedo of glacier ice, The Cryosphere, 16(4), 1197–1220,

846   https://doi.org/10.5194/tc-16-1197-2022, 2022.

847 Williamson, C. J., Anesio, A. M., Cook, J., Tedstone, A., Poniecka, E., Holland, A., Fagan,

848   D., Tranter, M., and Yallop, M.: Ice algal bloom development on the surface of the

849   Greenland Ice Sheet, FEMS Microbiol. Ecol., 94(3),

850   https://doi.org/10.1093/femsec/fiy025, 2018.

851 Wiscombe, W. J., and Warren, S. G.: A model for the spectral albedo of snow. I: Pure snow.

852   J. Atmos. Sci., 37(12), 2712–2733.

853   https://doi.org/10.1175/1520-0469(1980)037<2712:amftsa>2.0.co;2, 1980.

854 Ye, F., Cheng, Q., Hao, W., Yu, D., Ma, C., Liang, D., and Shen, H.: Reconstructing daily

855   snow and ice albedo series for Greenland by coupling spatiotemporal and

856   physics-informed models, Int. J. Appl. Earth Obs., 124, 103519,

857   https://doi.org/10.1016/j.jag.2023.103519, 2023.